Electric fields control water-gated proton transfer in cytochrome c oxidase

Saura, Patricia

2022-09-20

Saura , P , Riepl , D , Frey , D M , Wikström , M & Kaila , V R I 2022 , ' Electric fields control water-gated proton transfer in cytochrome c oxidase ' , Proceedings of the National Academy of Sciences of the United States of America , vol. 119 , no. 38 , e2207761119 . https://doi.org/10.1073/pna

http://hdl.handle.net/10138/355871
https://doi.org/10.1073/pnas.2207761119

PNAS RESEARCH ARTICLE | BIOPHYSICS AND COMPUTATIONAL BIOLOGY

Electric fields control water-gated proton transfer in cytochrome c oxidase

Patricia Saura[a], Daniel Riepl[a], Daniel M. Frey[a], Mårten Wikström[b], and Ville R. I. Kaila[a,1]

Edited by Harry Gray, California Institute of Technology, Pasadena, CA; received May 5, 2022; accepted August 18, 2022

Aerobic life is powered by membrane-bound enzymes that catalyze the transfer of electrons to oxygen and protons across a biological membrane. Cytochrome *c* oxidase (C*c*O) functions as a terminal electron acceptor in mitochondrial and bacterial respiratory chains, driving cellular respiration and transducing the free energy from O_2 reduction into proton pumping. Here we show that C*c*O creates orientated electric fields around a nonpolar cavity next to the active site, establishing a molecular switch that directs the protons along distinct pathways. By combining large-scale quantum chemical density functional theory (DFT) calculations with hybrid quantum mechanics/molecular mechanics (QM/MM) simulations and atomistic molecular dynamics (MD) explorations, we find that reduction of the electron donor, heme *a*, leads to dissociation of an arginine (Arg438)–heme a_3 D-propionate ion-pair. This ion-pair dissociation creates a strong electric field of up to 1 V $Å^{-1}$ along a water-mediated proton array leading to a transient proton loading site (PLS) near the active site. Protonation of the PLS triggers the reduction of the active site, which in turn aligns the electric field vectors along a second, "chemical," proton pathway. We find a linear energy relationship of the proton transfer barrier with the electric field strength that explains the effectivity of the gating process. Our mechanism shows distinct similarities to principles also found in other energy-converting enzymes, suggesting that orientated electric fields generally control enzyme catalysis.

PCET | bioenergetics | heme-copper oxidases | molecular simulations | QM/MM

Significance

Cytochrome *c* oxidase (C*c*O) powers aerobic life by reducing oxygen to water. This redox reaction creates a proton motive force across a biological membrane that drives the synthesis of adenosine triphosphate (ATP). C*c*O transfers the protons both across the membrane and to its active site responsible for oxygen reduction, but the gating principles of this reaction remain unsolved. Here we show that internal redox changes in C*c*O create orientated electric fields that sort the protons along the chemical and pumping pathways, while preventing back leakage reactions. These redox-triggered electric fields show distinct similarities to other energy-converting enzymes and may be a general principle of enzyme catalysis.

Cytochrome *c* oxidase (C*c*O) is the terminal enzyme of aerobic respiratory chains (1, 2). It catalyzes the reduction of molecular oxygen (O_2) to water, while pumping protons across the membrane (1–4), generating a chemiosmotic proton motive force (*pmf*) (5) that powers the synthesis of adenosine triphosphate (ATP) by F_oF_1-ATP synthase (6).

The mammalian C*c*O is composed of 13 subunits, forming 28 transmembrane helices (7) that are embedded within the inner mitochondrial membrane. The core subunits (subunits I–III) harbor the active site, a binuclear cluster (BNC) composed of heme a_3 and Cu_B. The BNC also comprises an unusual tyrosine residue (Tyr244, *Bos taurus* numbering), which is cross-linked to one of the histidine ligands (His240) of Cu_B (8, 9) (Fig. 1) and participates in the O_2 activation process (10). In the mammalian C*c*O, a low-spin heme A (heme *a*) lies within close distance (~6 Å edge-to-edge) to heme a_3 and serves as the electron donor or electron queueing site for the BNC (*cf.* ref. 11). A nonpolar cavity next to the BNC harbors water molecules (1, 12), which are produced as a result of the O_2 reduction process. Although these water molecules are not seen in the X-ray structures, presumably due to their high mobility, they are thought to be responsible for transferring the protons both to the BNC (chemical protons) and across the membrane (pumped protons) (13). The proton transfer reactions are driven by the electron transfer from heme *a* to the BNC (14). Heme *a*, in turn, receives the electrons from the dinuclear Cu_A center, located "above" heme *a*, and the soluble cytochrome *c*, which docks to subunit II at the positively charged side (P-side) of the membrane (Fig. 1).

Protons enter the active site via two distinct channels, the so-called D- and K-channels, which are named after the conserved residues Asp91 and Lys319 (*Bos taurus* numbering), respectively (15, 16). All pumped protons are transferred via the D-channel, whereas protons employed for the O_2 reduction process (chemical protons) originate from both channels (Fig. 1*A*). The proton pumping also involves a transient proton loading site (PLS), located next to the propionic groups of heme a_3 (1, 13, 17–20) that stores the proton before it is ejected to the P-side of the membrane.

The catalytic cycle of C*c*O (Fig. 1*B*) is initiated by binding of molecular O_2 to the reduced ferrous/cuprous form of the BNC in the so-called R state (Fe^{II}/Cu^{I}/Tyr-OH). This results in the A state (Fe^{III}-$O_2^{\bullet-}$/Cu^{I}/Tyr-OH), after which the O_2 ligand

Author affiliations: [a]Department of Biochemistry and Biophysics, Stockholm University, Stockholm 10691, Sweden; and [b]Institute of Biotechnology, University of Helsinki, 00014 Helsinki, Finland

Author contributions: V.R.I.K. designed research; P.S., D.R., D.M.F., and V.R.I.K. performed research; P.S. contributed new reagents/analytic tools; P.S., D.R., D.M.F., M.W., and V.R.I.K. analyzed data; and P.S., M.W., and V.R.I.K. wrote the paper.

The authors declare no competing interest.

This article is a PNAS Direct Submission.

[1]To whom correspondence may be addressed. Email: ville.kaila@dbb.su.se.

This article contains supporting information online at http://www.pnas.org/lookup/suppl/doi:10.1073/pnas.2207761119/-/DCSupplemental.

Published September 12, 2022.

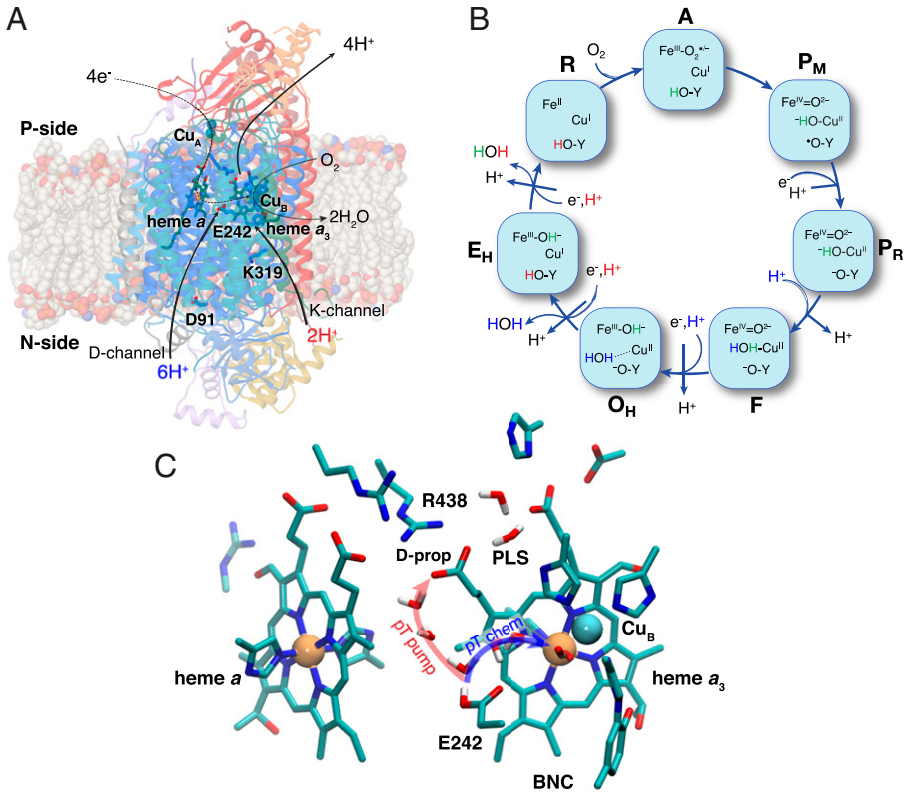

Fig. 1. Structure and function of C*c*O. (*A*) C*c*O from *Bos taurus* (PDB ID: 1V54) in its membrane environment (water and ions are omitted for visual clarity). C*c*O catalyzes the reduction of molecular O_2 to water with four sequential electron transfer steps from cytochrome *c* that couple to the transfer of four protons across the membrane. Protons enter the active site through the D- and K-channels. (*B*) Catalytic cycle of C*c*O: pumped protons are represented in black, chemical protons from D-channel in blue, and chemical protons from K-channel in red. (*C*) The C*c*O nonpolar cavity around the active site is formed by heme *a*, involved in electron transfer, and the BNC comprising heme a_3 and Cu_B, where the O_2 reduction takes place. This model shows the proton transfer pathways of a pumped proton (from Glu242 to D-propionate, in red) and a chemical proton (from Glu242 to the BNC, in blue).

receives four electrons from the BNC, the O–O bond is split, and the P_M state ($Fe^{IV}{=}O^{2-}/Cu^{II}$-OH^-/Tyr-$O^\bullet$) is formed. The subsequent four steps of the catalytic cycle result in re-reduction of the BNC. In each of these reaction steps, one electron is transferred to the BNC, coupling to proton transfer from the N-side of the membrane to the BNC (chemical protons), while another proton is transferred across the membrane to the P-side (pumped protons).

Reduction of the P_M state, by electron transfer from heme *a*, results in the P_R state ($Fe^{IV}{=}O^{2-}/Cu^{II}$-OH^-/Tyr-O^-), in a process that is linked to the transfer of a pumped and a chemical proton from the N-side via the D-channel, to the PLS and to the BNC, respectively. Reduction of the resulting "ferryl" F state ($Fe^{IV}{=}O^{2-}/Cu^{II}$-OH_2/Tyr-O^-) leads to a similar proton-coupled electron transfer (PCET) event with formation of the "oxidized" O_H state (Fe^{III}-OH^-..Cu^{II}/Tyr-O^-). Further reduction of $O_H \rightarrow E_H$ (Fe^{III}-OH^-/Cu^{I}/Tyr-OH) and onwards to the R state (Fe^{II}/Cu^{I}/Tyr-OH) involves similar redox-linked protonation of the PLS via the D-channel, while the chemical protons are taken up via the K-channel for reasons that remain partially unclear (Fig. 1*A*) (21–23).

Each one-electron transfer step along the catalytic cycle thus couples to transfer of one chemical proton to the BNC for completing the O_2 reduction chemistry, and another proton, first to the PLS, after which it is ejected to the P-side of the membrane. It is usually assumed that these four PCET events each take place by essentially the same mechanistic principles. It was proposed (12) based on picosecond classical molecular dynamics (MD) simulations (and later 60-ns MD simulations; *cf.* ref. 24) that the switch between pumped and chemical protons is controlled by the orientation of water molecules that is sensitive to the local electric field, which in turn, could be determined by the redox states of heme *a* and the BNC. Warshel and coworkers (25) found based on reactive force field calculations that the proton transfer energetics is dominated by large electrostatics barriers, but not the water orientation effect, which they considered "rather trivial" (25). Electrostatic effects were also found to be important for the proton transfer reactions from Glu242 to the propionate region of heme a_3 in reactive force field MD (26, 27) and semiempirical quantum mechanics/molecular mechanics (QM/MM) calculations (28), and coupled to conformational changes at Arg438 next to the D-propionate of heme a_3 (1, 15, 27, 29, 30). Although the involvement of water molecules as well as conformational changes within the active site pocket have been observed in several studies (12, 17, 19, 21, 24–32), the exact principles that create the required unidirectional proton gate still remain unsolved (17, 32, 33) and are likely to involve several contributions. The gating problem is thus highly challenging: its computational treatment requires an accurate description of the transition states linked to the proton transfer reactions (that are beyond the scope of classical atomistic MD simulations), treatment of the complex electronic structure of the binuclear Fe/Cu_B center and heme *a*, as well as accounting for the dynamics of the water molecules and surrounding amino acids. Moreover, the key intermediates involved have only been partially resolved experimentally due to challenges in probing the reaction cycle of C*c*O with the required high spatial (Å) and temporal (ns-ms) resolution, despite significant advances over the decades (14, 20, 34–38).

Here we focus on how electric field effects modulate proton transfer barriers near the active site and show that electric fields originating from the interheme electron transfer process control the proton transfer barriers along these distinct proton pathways. Based on multiscale molecular simulations that rely here on a first-principles density functional theory (DFT) treatment of the complete reactive system, we show that variations in intrinsic redox state–dependent electric fields explain the essential unidirectional gating of proton pumping in C*c*O, showing distinct similarities to other energy-converting enzyme complexes (39).

Results

Reduction of Heme *a* Induces Ion-Pair Dissociation. In order to probe the dynamics responsible for the proton transfer processes in the nonpolar cavity around the BNC, we first performed classical MD simulations of C*c*O from bovine heart mitochondria, embedded in a 1-palmitoyl-2-oleoyl-*sn*-glycero-3-phosphocholine (POPC)/palmitoyl-2-oleoyl-*sn*-glycero-3-phosphoethanolamine (POPE)/cardiolipin lipid membrane and solvated with water molecules and ions (*SI Appendix*, Fig. S1*A*). To study how the reduction of the electron-queuing heme *a* affects the proton transfer energetics, we modeled the active site prior (a^{red}/BNC^{ox}) and after (a^{ox}/BNC^{red}) the interheme electron transfer in the $P_M \rightarrow P_R$/F transition (Fig. 1, see *SI Appendix*, *SI Methods*), which couples to proton transfer both across the membrane and to the active site (1, 20). The simulations were initiated with a protonated Glu242, consistent with its high apparent pK_a value (32, 40).

When heme *a* is oxidized (a^{ox}), Arg438 forms an ion-pair with the D-propionate group of heme a_3, which remains in its closed conformation during the MD simulations (Fig. 2*A*). In contrast, upon reduction of heme *a* (a^{red}), mimicking the transfer of an electron from cytochrome *c*/Cu_A, Arg438 flips toward heme *a* by opening of the heme a_3 D-propionate/Arg438 ion-pair and establishing interactions with the D-propionate group of heme *a* (Fig. 2*A*, *cf.* also refs. 1, 30). The statistical validity of the redox state–dependent dynamics is also consistent with our free energy calculations, suggesting that heme *a* reduction favors the "open" heme a_3 D-propionate/Arg438 conformation by *ca.* 2 to 3 kcal mol^{-1} (*SI Appendix*, Fig. S2*F*). Our simulations suggest that the negative charge, created upon heme *a* reduction, interacts electrostatically with the positively charged Arg438, which in turn triggers the observed conformational change. While the structural difference between the closed and open ion-pair is rather subtle (Fig. 2*A*), we find here that it strongly modulates the energetics of the subsequent proton transfer steps (see below).

Ion-Pair Opening Triggers Protonation of the PLS. To study how the heme *a* reduction and dissociation of the ion-pair affect the proton transfer energetics, we constructed large (*ca.* 400 atoms) quantum chemical DFT models of the active site and its surroundings. The DFT models were based on the high-resolution X-ray structure of C*c*O from bovine heart mitochondria (41), but with added water molecules in the hydrophobic cavity, as predicted from our classical MD simulations (*SI Appendix*, Fig. S1*B*).

In the optimized DFT models, Glu242 is bridged to the D-propionate of heme a_3 via three water molecules in the cavity (Figs. 1*C* and 2*B*), while two water molecules (observed in the X-ray structure) also connect the D- and A-propionates of

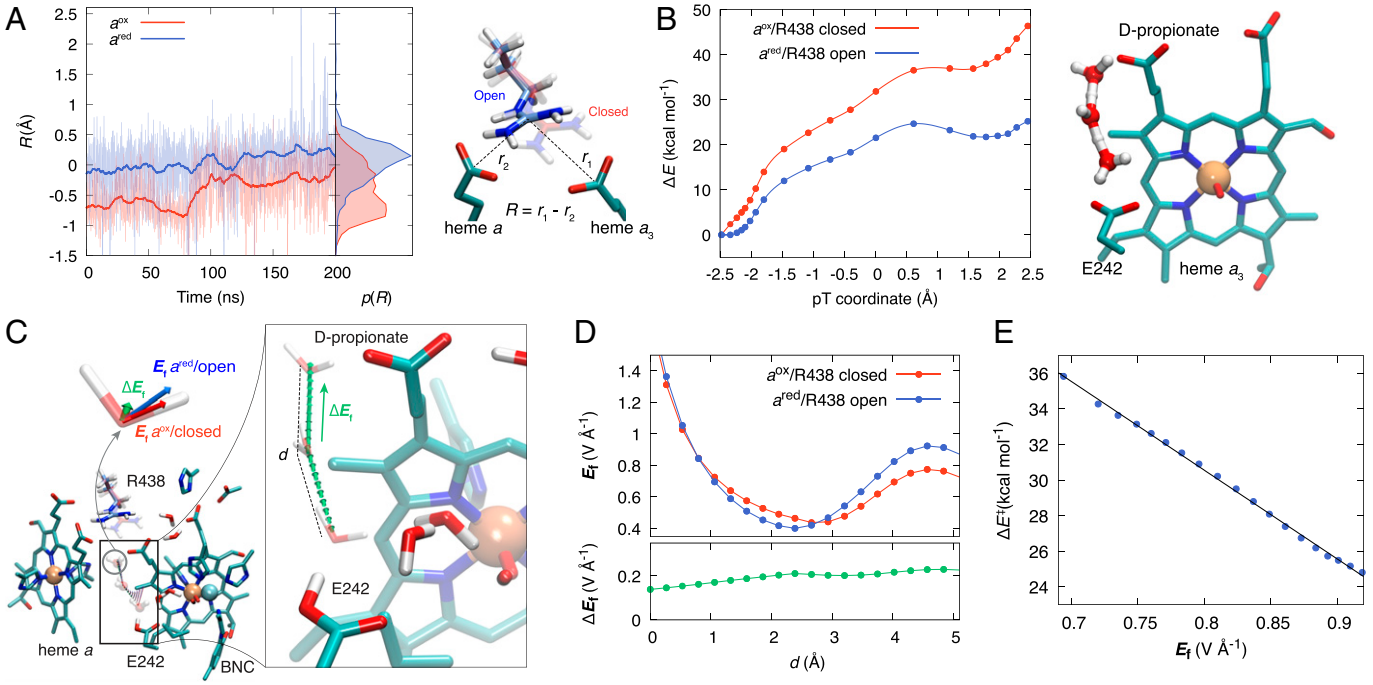

Fig. 2. Energetics and dynamics of the proton transfer along the pumping pathway. (*A*) Dynamics of the Arg438/heme a_3 D-propionate ion-pair in the P_M state with heme *a* oxidized (red) and heme *a* reduced (blue). The ion-pair conformation is represented by the reaction coordinate *R*, defined as the difference of distances of Arg438 to heme a_3 D-propionate (r_1) and Arg438 to heme *a* D-propionate (r_2). Reduction of heme *a* induces opening of the ion-pair. (*B*) (*Left*) Energetics of the proton transfer reaction from Glu242 to D-propionate (pumping pathway) in the P_M state with heme *a* oxidized/ion-pair closed (red) and heme *a* reduced/ion-pair open (blue). (*Right*) Structure of the protonated water intermediates along the proton wire, connecting Glu242 with the D-propionate. (*C*) Electric field vectors along the pumping pathway. Overall location (*Left*) and the resulting electric field difference vector [$\Delta E_f = E_f(a^{red}$/R438 open) − $E_f(a^{ox}$/R438 closed)] points in the direction of D-propionate (*Right*). See *SI Appendix*, Fig. S4 for detailed representations of individual electric field vectors. (*D*) Electric field strength along the vector connecting the water oxygen atoms along the proton transfer pathway. (*E*) The proton transfer barrier versus electric field at position of the protonated water cluster, calculated along the ion-pair dissociation scan, showing linear dependence between the barrier and field (see also *SI Appendix*, Fig. S3).

heme a_3 (*SI Appendix*, Fig. S2*A*). Additionally, three water molecules may form a hydrogen-bonded array, connecting Glu242 to the hydroxy ligand of Cu_B, consistent with previous work (12, 24, 26, 32, 42–45). The orientation of these water chains has been suggested to respond to the redox state of the enzyme (1, 12, 21, 24, but *cf.* also refs. 25, 26). To study the effect of heme *a* reduction on the proton transfer toward the PLS, we included the heme *a* cofactor and its surrounding residues in the DFT models and modeled the system in its oxidized or reduced states with the respective open/closed states of the Arg438-propionate ion-pair (see *Materials and Methods*). Inclusion of heme *a* with the BNC allowed us to model possible polarization effects at the electronic structure level.

Our DFT models suggest that the water-mediated proton transfer from Glu242 to the D-propionate of heme a_3 takes place via a stepwise Grotthuss-type transfer process (46), with protonated water intermediates (H_3O^+ and $H_5O_2^+$) stabilized by the carboxylic groups of the glutamate and propionate (Fig. 2*B*), as well as by cation–π interactions with Trp126 (*SI Appendix*, Fig. S2*B*), consistent with experimental data supporting the involvement of Trp126 in the proton-pumping process (47).

When heme *a* is in the oxidized state and the ion-pair remains in the closed conformation (Fig. 2*A*), the proton transfer along the pump pathway has a high barrier (>30 kcal mol^{-1}) in the DFT models that is inaccessible on the millisecond turnover of C*c*O. The strong electrostatic stabilization of the anionic D-propionate by Arg438 in the closed ion-pair prevents the protonation of the former. In stark contrast, when heme *a* was reduced, which favors the opened ion-pair according to our MD simulations (Fig. 2*A*; *cf.* also ref. 30), the proton transfer along the pump pathway is stabilized by >15 kcal mol^{-1} (Fig. 2*B*). Based on further analysis (*SI Appendix*, Fig. S2), we find that opening of the Arg438/D-propionate ion-pair has a stronger effect on this barrier modulation as compared to the heme *a* reduction alone, although both effects are strongly coupled to one another (Fig. 2*A*). We obtain similar redox state–dependent proton transfer energetics also in DFT-based hybrid QM/MM models, where the reactive quantum chemically modeled region is further polarized by the classical (force-field) description of the surroundings (*SI Appendix*, Figs. S3 *A* and *B*).

To elucidate the physical basis of this drastic barrier modulation, we computed the electric fields along the pump pathway in the different redox and conformational states (Fig. 2 *C* and *D*). Reduction of heme *a* alone (without the Arg438 flip) does not show a drastic increase in the magnitude of the electric field, but the resulting field vectors ($\Delta \boldsymbol{E_f} = \boldsymbol{E_f}(\text{red})\text{-}\boldsymbol{E_f}(\text{ox})$; $\boldsymbol{E_f}$, electric field) point in the direction of heme *a*, that is, perpendicular to the proton transfer pathway (*SI Appendix*, Figs. S4*A* and S6*A*). This perpendicular electric field component gives rise to a displacing force on the positively charged Arg438 ($\boldsymbol{F} = q\Delta\boldsymbol{E_f}$), inducing its movement toward heme *a*, consistent with our MD simulations. The Arg438 flip leaves an unshielded negative charge on the D-propionate of heme a_3, which, in turn, induces an electric field orientated along the direction of the proton pump pathway (*SI Appendix*, Figs. S4*B* and S6 *B* and *D*). Interestingly, the combined field effect arising from heme *a* reduction and the Arg438 flip creates a rather strong electric field of *ca.* 0.2 V $Å^{-1}$ along the pump pathway that increases up to 1 V $Å^{-1}$ near the D-propionate group (Fig. 2 *C* and *D*). This electric field correlates linearly with a decrease of the proton transfer barrier by stabilizing the protonated water cluster (Fig. 2*E* and *SI Appendix*, Fig. S6).

We next probed if the electric field variations arising from the ion-pair opening could affect the vibrational frequencies of the groups involved in the proton transfer reaction via the vibrational Stark effect (VSE) (48) (see *Materials and Methods*). Interestingly, we observe a sharp vibrational band in the computed infrared spectra, corresponding to the O–H bond stretching of the Glu242 carboxyl group (*SI Appendix*, Fig. S7*A*) that shifts by *ca.* 10 cm^{-1} upon opening of the ion-pair, with a linear dependency of the vibrational frequency on the electric field strength (*SI Appendix*, Fig. S7 *B–E*). These findings suggest that Stark probes, for example, with nitrile groups (49), could be used at this or nearby sites to experimentally validate the predicted global electric field effects near the BNC.

After proton transfer to the D-propionate of heme a_3, it has been suggested that the proton is transiently stored at or near the propionate region, before it is ejected to the P-side of the membrane (see, e.g., refs. 1, 17). The exact location of this PLS remains unknown, but it could comprise, for example, the A-propionate of heme a_3, or reside between the two propionic groups (17–19, 50). To obtain further insight into the protonation of the PLS, we estimated the energetics of the proton transfer from the D-propionate to the A-propionate of heme a_3 via the two intervening water molecules (*SI Appendix*, Fig. S8). Our calculations suggest that this process has comparable energetics to the previous proton transfer reaction (from Glu242 to the D-propionate) when the ion-pair is open (Fig. 2*B* and *SI Appendix*, Fig. S8). However, upon formation of the closed ion-pair (see below), the proton transfer barrier from the D- to the A-propionate significantly decreases (*SI Appendix*, Fig. S8*A*), suggesting that the "back-flip" of the Arg438, triggered by the electron transfer to the BNC, could further stabilize the protonated PLS (PLSH) and prevent back leakage of the proton from the PLSH to Glu242 (see *Discussion*). Due to the electrostatic nature of the electric field effects and the proximity of PLS to heme *a*/BNC, we expect that the results are likely to apply also if the PLS comprises a shared site "above" heme a_3, as suggested by Gunner and coworkers (18, 31, 52; see also refs. 1, 17, 19, 51). Moreover, although not studied here, dehydration of the contacts between the P-side and the BNC (53) is further expected to enhance the predicted gating effects by increasing the reaction barriers for the leak reaction.

Reduction of the BNC Drives Proton Transfer along the Chemical Pathway. We next investigated electric field effects underlying the proton transfer reactions along the chemical pathway from Glu242 to the BNC. We modeled the reactions following the reprotonation of Glu242 through the proton-conducting D-channel (15, 16), and by also considering the influence of the PLSH (see above). Our DFT calculations suggest that protonation of the PLS increases the electron affinity of the BNC by *ca.* 350 mV (8 kcal mol^{-1}, *SI Appendix*, Table S1), which favors the electron transfer from heme *a* to the BNC, consistent with the tight coupling between the proton and electron transfer reactions (1, 13). Prior to the reduction of the BNC (the P_M state), the proton transfer from Glu242 to the hydroxy-ligand of Cu_B has an energy barrier of *ca.* 10 kcal mol^{-1}, and the reaction is weakly endergonic. Similarly as for the pump pathway, the reaction proceeds via a Grotthuss mechanism with H_3O^+/Zundel ion intermediates (46). Reduction of the BNC (P_R state), which is favored by protonation of the PLS, lowers the proton transfer energy barrier to around 8 kcal mol^{-1} while increasing the thermodynamic driving force to −2 kcal mol^{-1} (Fig. 3*A*). This effect arises from an increase in the electric field by up to 0.2 V $Å^{-1}$ along the chemical proton pathway, with the resulting field vectors orientated along the direction of the water wire toward Cu_B (Fig. 3 *B* and *C* and *SI Appendix*, Fig. S5).

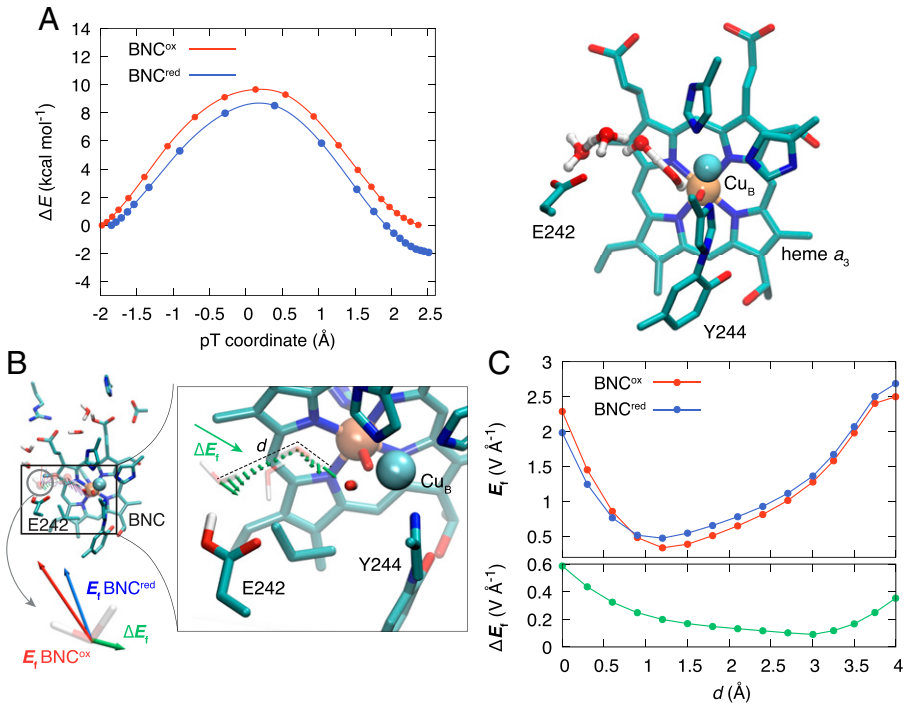

Fig. 3. Energetics of the proton transfer reaction along the chemical pathway. (*A*) Energy profiles for the chemical proton transfer process with oxidized (BNC^{ox}/P_M) and reduced (BNC^{red}/P_R) BNC and a protonated PLSH. (*Right*) Structure of the protonated water wire connecting Glu242 to Cu_B at the transition state. (*B*) Electric field vectors along the *chemical* proton transfer pathway. (*Left*) Overall location. (*Right*) Resulting electric field difference vector [$\Delta E_f = E_f(BNC^{red}) - E_f(BNC^{ox})$] is pointing in the direction of the BNC. See *SI Appendix*, Fig. S5 for detailed representations of individual electric field vectors. (*C*) Electric field strengths along the vector connecting the water oxygen atoms along the chemical proton pathway.

These findings are also supported by our QM/MM calculations, where the reduction of the BNC lowers the barrier and increases the driving force by *ca.* 2 to 3 kcal mol^{-1} (*SI Appendix*, Fig. S3 *C* and *D*). Interestingly, during DFT-based QM/MM MD simulations, we observe that the O-H dipoles of the water chain spontaneously flip along the electric field vectors pointing toward the reduced BNC (*SI Appendix*, Fig. S3*E*), whereas when the BNC is modeled in the oxidized state, the water dipoles point in the opposite direction during the QM/MM MD (*SI Appendix*, Fig. S3*E*), resembling the behavior observed in classical MD simulations (1, 12, 19, 24).

Discussion

In this work, we have studied the gating mechanism by which C*c*O transfers protons across the membrane and to the active site (BNC). In the oxidative phase of the catalytic cycle (P→F→O_H), Glu242, located at the end of the D-channel, sorts these pumped and chemical protons by a tightly linked electron transfer process. We proposed here that the electron transfer between heme *a* and the BNC creates strong orientated electric fields that control the proton transfer barriers along these distinct pathways that in turn minimize back-leakage reactions.

Reduction of heme *a* was found to create an orientated electric field that leads to the dissociation of the Arg438/D-propionate ion-pair by displacing the positively charged Arg438 toward the D-propionate group of heme *a* (Fig. 4*A*). This in turn creates an electric field in the direction of the water array that connects Glu242 to the PLS, located in the propionate region of heme a_3, and lowers the proton transfer barrier along the pump pathway (Fig. 4*B*). The deprotonated Glu242 swings back toward the D-channel (32; *cf.* also refs. 27, 31, 54, 55) and picks up a second proton due to its high pK_a (15). Such multiple conformations of Glu242 were recently observed, based on asymmetric reconstruction of the cryo-electron microscopy maps, in a refined high-resolution structure of an actinobacterial cytochrome *bcc-aa*$_3$ supercomplex (56, PDB ID: 7QHM), which also showed subtle conformational changes at the heme a_3 D-propionate/Arg438 region. Interestingly, mutation of Glu242 to Gln also induces conformational changes at the D-propionate/Arg438 site, supporting the electrostatic coupling between the proton donor and acceptor (57).

Interestingly, Goyal et al. (31) found that the pK_a of Glu242 could also be modulated by the hydration state of the nonpolar cavity itself. Although this effect is not studied here, we note that Glu242 is affected by both the redox state and hydration state of the nonpolar cavity in our classical MD simulations (*SI Appendix*, Fig. S10) and could provide an additional gating effect in preventing back-leak reactions, as suggested in previous studies (31, 32, 53).

PLSH strongly increases the electron affinity of the BNC (*SI Appendix*, Table S1), which favors electron transfer from heme *a*, and, in turn, creates an electric field in the direction of the BNC (Fig. 4*C*). This electric field lowers the proton transfer barrier along the hydrogen-bonded water array that connects Glu242 to the oxygenous ligand of Cu_B (Fig. 4*C*). The oxidation of heme *a* favors reassociation of the Arg438/D-propionate ion-pair, which could help in stabilizing the protonated PLS and preventing back-leakage of the proton toward the anionic Glu242—in part as the proton would need to pass the positively charged Arg438, but also as the oxidized heme *a* leads to an increase of the proton transfer barrier along the pump pathway (see also ref. 33), even if the hydration state of the nonpolar cavity would increase upon protonation of the PLS (*cf.* ref. 31). The anionic Glu242 now flips toward the D-channel (32, but *cf.* also refs. 27, 31, 54) and becomes rapidly reprotonated. Indeed, mutations of conserved residues along the D-channel (e.g., N139D *Rhodobacter sphaeroides* numbering) (58), which

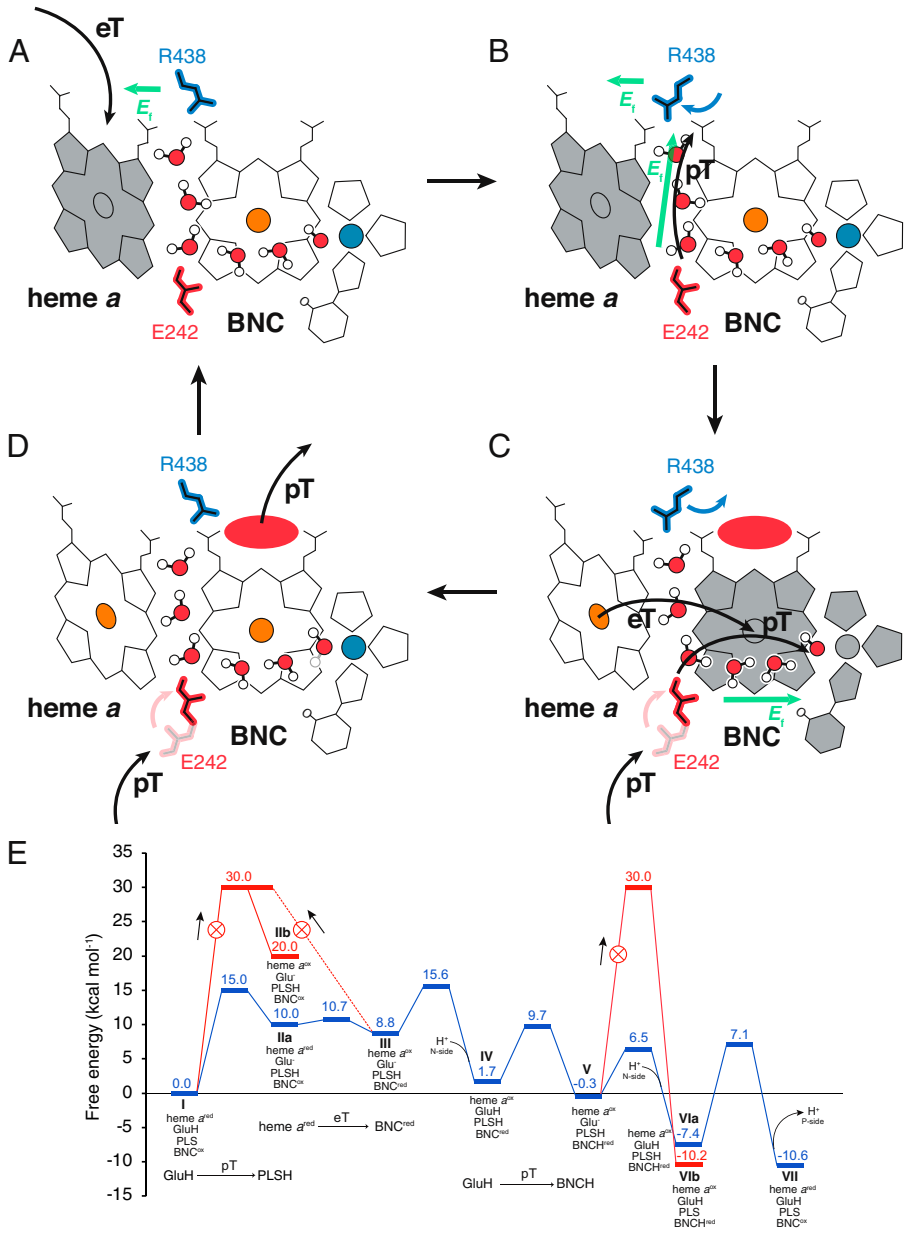

Fig. 4. Proposed gating principles in CcO. Reduced cofactors are colored in gray, and protonated PLSH is represented by a red ellipse. (*A*) Electron transfer (eT) from cytochrome *c* to heme *a* creates an electric field (E_f) in the direction of heme *a* that causes dissociation of Arg438 from heme a_3. (*B*) The Arg438 flip leaves the negative D-propionate exposed that creates an electric field along the Glu242→D-propionate direction that induces the transfer of a proton toward the PLS. (*C*) The PLSH state increases the electron affinity of the BNC. Electron transfer from heme *a* to the BNC creates an electric field toward Cu_B facilitating the proton transfer from Glu242 (with prior Glu242 reprotonation from the D-channel). (*D*) Heme *a* oxidation causes Arg438 to close back toward the PLSH that pushes the stored proton to the P-side bulk and regenerates the state to the next PCET cycle. (*E*) Free energy diagram of the redox-driven proton pumping steps. The values are based on the present calculations and experimental data (see *SI Appendix, Extended Methods*).

slow down the reprotonation of Glu242, result in loss of the pumping activity while retaining the O_2 reductase activity. Protonation and reduction of the BNC lowers the proton affinity of the PLSH, and the pumped proton is then ejected to the aqueous P-side of the membrane (Fig. 4*D*), while reprotonation of Glu242 by proton uptake from the N-side via the D-channel restores the residue for the next step of the catalytic cycle.

The free energy diagram for these redox-driven proton transfer steps, derived based on the present calculations and experimental data, is shown in Fig. 4*E* (see also *SI Appendix, Extended Methods*). The thermodynamic driving force for a single proton pumping step is around −10.6 kcal mol^{-1} (Fig. 4*E*, state VII, *SI Appendix, Extended Materials and Methods*; *cf.* also ref. 59), which is sufficient to translocate two charges ($2H^+/e^-$) across the membrane at a 220 mV *pmf* (ΔG = 5.1 kcal mol^{-1}/H^+). The heme *a* reduction significantly lowers the barrier for the initial endergonic proton transfer from Glu242 to the PLS (Fig. 4*E*, step I→IIa) by the electric field effects discussed above, creating a high kinetic barrier for the backflow of the proton from the PLS to Glu242 (Fig. 4*E*, step III→I). We note that the high pK_a of Glu242 provides downhill steps (Fig. 4*E*, III→IV and V→VI) that favor the rapid reprotonation of the carboxylate, which could be further enhanced by conformational switching of the Glu242 (*cf.* refs. 32, 56). Importantly, steps V→VIa/VII, which couple to the release of the proton to the P-side bulk, are highly vulnerable to leaks, as the rather high barrier ($\Delta G^{\ddagger}$ = 14.5 kcal mol^{-1}) for releasing the PLS proton to the P-side competes with the thermodynamically favored backflow of the proton to Glu242

(Fig. 4*E*, state VIb). To this end, the Arg-backflip induced by the heme *a* oxidation and the altered field effects along the pump pathway are expected to create a high kinetic barrier (Fig. 4*E*, state V→VIb) that prevents this short-circuit reaction and favors instead the rapid reprotonation of Glu242 form the D-channel. In our kinetic model based on this free energy diagram (*SI Appendix*, Fig. S9), we indeed observe a significant increase of this backleak reaction when the reprotonation barriers of the Glu242 competes with that of the PLSH→Glu242 back-transfer (V→VIb) (*SI Appendix*, Fig. S9), consistent with the experimental data on the D-channel mutants (58), discussed above.

Electric field variations can be experimentally measured via the vibrational Stark effect (48), which results from shifted vibrational energy levels and transition dipoles. Recent spectroscopic studies suggested that a CO probe bound to heme a_3 (60) experiences a field variation of around 2.9 MV cm^{-1} (0.03 V $Å^{-1}$) upon reduction, which is consistent with our estimates of the field effect in the vicinity of the BNC (Fig. 3*C*). Moreover, spectroscopic studies have shown redox-dependent shifts in the 1742 cm^{-1} band assigned to the C=O vibrations of the carboxyl group of Glu242 (61–63). By calculation of the vibrational spectrum based on DFT models, we found that the electric field variations induced by the Arg438 dissociation indeed induce a linear shift of the vibrational frequencies connected to the Glu carboxyl vibrations, although the region contains several coupled vibrations that can be difficult to assign experimentally (*SI Appendix*, Fig. S7). Nevertheless, these findings suggest that that the vibrational shifts of residues near the active site could be used to experimentally validate the proposed electric field–triggered proton gating principles.

The redox-triggered electric field variations could direct the gating in all steps of the catalytic cycle (Fig. 1*B*), although the K-channel is employed for the uptake of chemical protons in the reductive phase (O_H→E_H→R) (15,16). The electric field effects triggered by heme *a* reduction and Arg438-propionate ion-pair dissociation are expected to lead to a radial increase in the field toward the BNC upon its reduction. During the oxidative phase (P_M→F→O_H) these changes are expected to create an electric field that points from Glu242 to Cu_B similar as in the P_M → P_R step studied here due to the similar overall change in density around the Cu and the heme a_3 Fe. However, the weak water ligand on Cu_B formed toward the reductive phase and its subsequent dissociation (33, 64, 65) may destabilize the proton-conducting water chain between Glu242 and Cu_B and instead favor proton uptake via the K-channel (21, 23), due to increase of the pK_a of Tyr244 (21, 64, 66, 67).

The functional elements around the heme *a*/BNC region responsible for the proposed field-driven proton gating are fully conserved within the A-type of C*c*O, which is present in mitochondria and many bacteria. Interestingly, the bacterial C-type oxidases (cytochrome cbb_3), which do not employ the D-channel for proton uptake, have a Ca^{2+} ion replacing the Arg438 (68). Cytochrome cbb_3 pumps protons with a full stoichiometry of 1 H^+/e^- (69) at optimal conditions of no opposing protonmotive force. However, the pathway leading to the PLS uses the K-channel analog behind the heme b_3 to the propionate region (70–72). The high sensitivity of pumping efficiency in cbb_3 to even low values of protonmotive force might reflect the absence of the effective gating function of the Arg438-propionate pair in the type A oxidases.

The redox-driven electric field variations driving and controlling the PCET process may also be applicable to other energy-converting enzymes (39, 73). In the respiratory complex I, quinone reduction and diffusion to a second binding site has been suggested to trigger opening of conserved ion-pairs that modulate proton transfer barriers across the membrane (74). A similar redox-driven ion-pair dissociation was also recently described in Photosystem II (75), which drives the substrate water deprotonation via electric field effects. The role of the electric field in directing catalysis has recently gained significant attention also for the control of chemical catalysts (76). We suggest that the described electric field effects are generally employed as molecular principles in biological energy conversion (39).

Conclusion

Here we have shown how redox-triggered electric fields effects control the PCET reactions within the active site of C*c*O. Strong orientated electric fields of up to 1 V $Å^{-1}$ form along the proton-conducting water wires in the direction of the proton transfer reactions. Glu242, a key conserved residue at the end of the proton-conducing D-channel, was found to establish a bifurcation switch that gates the protons either to a PLS (pumped protons) or to the binuclear Fe/Cu site (BNC; the chemical protons) via the redox-triggered field modulations. These electric fields modulate the proton transfer barriers and thermodynamics, creating gates and locks that could form the basis for unidirectional proton pumping without dissipation of energy. The electric field effects control the proton transfer barriers, by the same principles that the water arrays tend to orientate toward the chemical/pumping pathway, as observed in early MD studies of the process (12). It is important to note that such catalytically relevant electric fields must rely on a precise structure, which may be one reason for why the structural organization of the two hemes of C*c*O enzymes is fully conserved. By comparing our findings to mechanistic principles proposed in other enzymes (39, 74, 75), we further suggest that electric field effects are employed as general mechanisms to control catalysis and protonation dynamics in energy-converting enzymes.

Materials and Methods

The energetics of the proton transfer reactions along the pumping and chemical pathways were studied using large-scale DFT models and QM/MM calculations, constructed based on the crystal structure of the bovine CcO (PDB ID: 1V54) (41). The DFT models comprised heme a_3/Cu_B, heme *a*, and surrounding protein residues, with water molecules along the pumping/chemical pathways derived from classical MD simulations (19). The DFT models comprised 260 to 400 atoms. Geometries and reaction pathways were optimized at the BP86-D3/def2-SVP/def2-TZVP(Fe,Cu)/$\varepsilon = 4$ level, with energetics and electric fields computed at the B3LYP-D3/def2-SVP/def2-TZVP(Fe,Cu) level (77, 78). QM/MM models were constructed based on classically relaxed MD snapshots with the QM region (125 atoms) modeled at the B3LYP-D3/def2-SVP/def2-TZVP(Cu) level, and coupled to the MM surroundings (55,000 atoms), modeled at the CHARMM36 level (79), via the link atom approach. Classical MD simulations of the bovine CcO, embedded in a POPC/POPE/cardiolipin membrane, TIP3P water, and 150 mM NaCl, with *ca.* 260,000 atoms, were carried out using the CHARMM36 force field together with DFT-based parameters of the cofactors (80). The MD simulations were performed in an *NPT* (1 atm/310 K) ensemble, with a 2 fs integration time step, and using PME for modeling long-range electrostatics. The free energy of the Arg438/heme a_3 D-propionate opening was studied using replica-exchange umbrella sampling (REUS) calculations, using the same parameters as in the unbiased MD simulations. All DFT calculations were performed with TURBOMOLE v7.2–7.5 (81), QM/MM calculations with CHARMM v38 (82) and TURBOMOLE v7.2–7.5 (81), coupled by a Python interface (83), and classical MD simulations with NAMD v2.14 and NAMD v3.0 (84). See *SI Appendix, Extended Materials and Methods* for a detailed description of all methods.

Data, Materials, and Software Availability. All study data are included in the article and/or supporting information.

ACKNOWLEDGMENTS. This work was funded by the Knut and Alice Wallenberg Foundation (2019.0251 and 2019.0043 to V.R.I.K.). V.R.I.K. also acknowledges support from the German Research Foundation (DFG) via the Collaborative Research Centre (SFB1078) as Mercator Fellow. Computational resources were provided by the Swedish National Infrastructure for Computing (SNIC 2021/1-40, SNIC 2022/1-29) at the Center of High-Performance Computing (PDC), and by the Leibniz-Rechenzentrum. M.W. was supported by the Institute of Biotechnology, University of Helsinki.

1. V. R. I. Kaila, M. I. Verkhovsky, M. Wikström, Proton-coupled electron transfer in cytochrome oxidase. *Chem. Rev.* **110**, 7062–7081 (2010).
2. V. R. I. Kaila, M. Wikström, Architecture of bacterial respiratory chains. *Nat. Rev. Microbiol.* **19**, 319–330 (2021).
3. M. K. Wikström, Proton pump coupled to cytochrome *c* oxidase in mitochondria. *Nature* **266**, 271–273 (1977).
4. M. Wikström, K. Krab, V. Sharma, Oxygen activation and energy conservation by cytochrome *c* oxidase. *Chem. Rev.* **118**, 2469–2490 (2018).
5. P. Mitchell, Coupling of phosphorylation to electron and hydrogen transfer by a chemi-osmotic type of mechanism. *Nature* **191**, 144–148 (1961).
6. M. Yoshida, E. Muneyuki, T. Hisabori, ATP synthase–A marvellous rotary engine of the cell. *Nat. Rev. Mol. Cell Biol.* **2**, 669–677 (2001).
7. T. Tsukihara *et al.*, The whole structure of the 13-subunit oxidized cytochrome *c* oxidase at 2.8 Å. *Science* **272**, 1136–1144 (1996).
8. S. Yoshikawa *et al.*, Redox-coupled crystal structural changes in bovine heart cytochrome *c* oxidase. *Science* **280**, 1723–1729 (1998).
9. G. Buse, T. Soulimane, M. Dewor, H. E. Meyer, M. Blüggel, Evidence for a copper-coordinated histidine-tyrosine cross-link in the active site of cytochrome oxidase. *Protein Sci.* **8**, 985–990 (1999).
10. D. A. Proshlyakov, M. A. Pressler, G. T. Babcock, Dioxygen activation and bond cleavage by mixed-valence cytochrome *c* oxidase. *Proc. Natl. Acad. Sci. U.S.A.* **95**, 8020–8025 (1998).
11. G. T. Babcock, M. Wikström, Oxygen activation and the conservation of energy in cell respiration. *Nature* **356**, 301–309 (1992).
12. M. Wikström, M. I. Verkhovsky, G. Hummer, Water-gated mechanism of proton translocation by cytochrome *c* oxidase. *Biochim. Biophys. Acta* **1604**, 61–65 (2003).
13. M. Wikström, V. Sharma, V. R. I. Kaila, J. P. Hosler, G. Hummer, New perspectives on proton pumping in cellular respiration. *Chem. Rev.* **115**, 2196–2221 (2015).
14. I. Belevich, M. I. Verkhovsky, M. Wikström, Proton-coupled electron transfer drives the proton pump of cytochrome *c* oxidase. *Nature* **440**, 829–832 (2006).
15. P. Brzezinski, Redox-driven membrane-bound proton pumps. *Trends Biochem. Sci.* **29**, 380–387 (2004).
16. R. B. Gennis, Coupled proton and electron transfer reactions in cytochrome oxidase. *Front. Biosci.* **9**, 581–591 (2004).
17. V. R. I. Kaila, V. Sharma, M. Wikström, The identity of the transient proton loading site of the proton-pumping mechanism of cytochrome *c* oxidase. *Biochim. Biophys. Acta* **1807**, 80–84 (2011).
18. J. Lu, M. R. Gunner, Characterizing the proton loading site in cytochrome *c* oxidase. *Proc. Natl. Acad. Sci. U.S.A.* **111**, 12414–12419 (2014).
19. S. Supekar, A. P. Gamiz-Hernandez, V. R. I. Kaila, A protonated water cluster as a transient proton-loading site in cytochrome *c* oxidase. *Angew. Chem. Int. Ed. Engl.* **55**, 11940–11944 (2016).
20. I. Belevich, D. A. Bloch, N. Belevich, M. Wikström, M. I. Verkhovsky, Exploring the proton pump mechanism of cytochrome *c* oxidase in real time. *Proc. Natl. Acad. Sci. U.S.A.* **104**, 2685–2690 (2007).
21. S. Supekar, V. R. I. Kaila, Dewetting transitions coupled to K-channel activation in cytochrome *c* oxidase. *Chem. Sci. (Camb.)* **9**, 6703–6710 (2018).
22. H. Lepp, E. Svahn, K. Faxén, P. Brzezinski, Charge transfer in the K proton pathway linked to electron transfer to the catalytic site in cytochrome *c* oxidase. *Biochemistry* **47**, 4929–4935 (2008).
23. A. Wolf *et al.*, The redox-coupled proton-channel opening in cytochrome *c* oxidase. *Chem. Sci. (Camb.)* **11**, 3804–3811 (2020).
24. V. Sharma, G. Enkavi, I. Vattulainen, T. Róg, M. Wikström, Proton-coupled electron transfer and the role of water molecules in proton pumping by cytochrome *c* oxidase. *Proc. Natl. Acad. Sci. U.S.A.* **112**, 2040–2045 (2015).
25. A. V. Pisliakov, P. K. Sharma, Z. T. Chu, M. Haranczyk, A. Warshel, Electrostatic basis for the unidirectionality of the primary proton transfer in cytochrome *c* oxidase. *Proc. Natl. Acad. Sci. U.S.A.* **105**, 7726–7731 (2008).
26. R. Liang, J. M. J. Swanson, Y. Peng, M. Wikström, G. A. Voth, Multiscale simulations reveal key features of the proton-pumping mechanism in cytochrome *c* oxidase. *Proc. Natl. Acad. Sci. U.S.A.* **113**, 7420–7425 (2016).
27. T. Yamashita, G. A. Voth, Insights into the mechanism of proton transport in cytochrome *c* oxidase. *J. Am. Chem. Soc.* **134**, 1147–1152 (2012).
28. P. Goyal, S. Yang, Q. Cui, Microscopic basis for kinetic gating in cytochrome *c* oxidase: Insights from QM/MM analysis. *Chem. Sci. (Camb.)* **6**, 826–841 (2015).
29. Y. Song, E. Michonova-Alexova, M. R. Gunner, Calculated proton uptake on anaerobic reduction of cytochrome *C* oxidase: Is the reaction electroneutral? *Biochemistry* **45**, 7959–7975 (2006).
30. M. Wikström *et al.*, Gating of proton and water transfer in the respiratory enzyme cytochrome *c* oxidase. *Proc. Natl. Acad. Sci. U.S.A.* **102**, 10478–10481 (2005).
31. P. Goyal, J. Lu, S. Yang, M. R. Gunner, Q. Cui, Changing hydration level in an internal cavity modulates the proton affinity of a key glutamate in cytochrome *c* oxidase. *Proc. Natl. Acad. Sci. U.S.A.* **110**, 18886–18891 (2013).
32. V. R. I. Kaila, M. I. Verkhovsky, G. Hummer, M. Wikström, Glutamic acid 242 is a valve in the proton pump of cytochrome *c* oxidase. *Proc. Natl. Acad. Sci. U.S.A.* **105**, 6255–6259 (2008).
33. M. R. A. Blomberg, P. E. M. Siegbahn, The mechanism for proton pumping in cytochrome *c* oxidase from an electrostatic and quantum chemical perspective. *Biochim. Biophys. Acta* **1817**, 495–505 (2012).
34. K. Faxén, G. Gilderson, P. Ädelroth, P. Brzezinski, A mechanistic principle for proton pumping by cytochrome *c* oxidase. *Nature* **437**, 286–289 (2005).
35. M. Wikström, M. I. Verkhovsky, Mechanism and energetics of proton translocation by the respiratory heme-copper oxidases. *Biochim. Biophys. Acta* **1767**, 1200–1214 (2007).
36. S. Shimada *et al.*, Complex structure of cytochrome *c*-cytochrome *c* oxidase reveals a novel protein-protein interaction mode. *EMBO J.* **36**, 291–300 (2017).
37. I. Ishigami *et al.*, Snapshot of an oxygen intermediate in the catalytic reaction of cytochrome *c* oxidase. *Proc. Natl. Acad. Sci. U.S.A.* **116**, 3572–3577 (2019).
38. F. Kolbe *et al.*, Cryo-EM structures of intermediates suggest an alternative catalytic reaction cycle for cytochrome *c* oxidase. *Nat. Commun.* **12**, 6903 (2021).
39. V. R. I. Kaila, Resolving chemical dynamics in biological energy conversion: Long-range proton-coupled electron transfer in respiratory complex I. *Acc. Chem. Res.* **54**, 4462–4473 (2021).
40. G. Brändén, A. S. Pawate, R. B. Gennis, P. Brzezinski, Controlled uncoupling and recoupling of proton pumping in cytochrome *c* oxidase. *Proc. Natl. Acad. Sci. U.S.A.* **103**, 317–322 (2006).
41. T. Tsukihara *et al.*, The low-spin heme of cytochrome *c* oxidase as the driving element of the proton-pumping process. *Proc. Natl. Acad. Sci. U.S.A.* **100**, 15304–15309 (2003).
42. M. H. M. Olsson, A. Warshel, Monte Carlo simulations of proton pumps: On the working principles of the biological valve that controls proton pumping in cytochrome *c* oxidase. *Proc. Natl. Acad. Sci. U.S.A.* **103**, 6500–6505 (2006).
43. E. Fadda, C.-H. Yu, R. Pomès, Electrostatic control of proton pumping in cytochrome *c* oxidase. *Biochim. Biophys. Acta* **1777**, 277–284 (2008).
44. N. Ghosh, X. Prat-Resina, M. R. Gunner, Q. Cui, Microscopic pK_a analysis of Glu286 in cytochrome *c* oxidase (*Rhodobacter sphaeroides*): Toward a calibrated molecular model. *Biochemistry* **48**, 2468–2485 (2009).
45. X. Zheng, D. M. Medvedev, J. Swanson, A. A. Stuchebrukhov, Computer simulation of water in cytochrome *c* oxidase. *Biochim. Biophys. Acta* **1557**, 99–107 (2003).
46. N. Agmon, The Grotthuss mechanism. *Chem. Phys. Lett.* **244**, 456–462 (1995).
47. C. Ribacka *et al.*, An elementary reaction step of the proton pump is revealed by mutation of tryptophan-164 to phenylalanine in cytochrome *c* oxidase from *Paracoccus denitrificans*. *Biochemistry* **44**, 16502–16512 (2005).
48. S. D. Fried, S. G. Boxer, Measuring electric fields and noncovalent interactions using the vibrational stark effect. *Acc. Chem. Res.* **48**, 998–1006 (2015).
49. J. B. Weaver, J. Kozuch, J. M. Kirsh, S. G. Boxer, Nitrile infrared intensities characterize electric fields and hydrogen bonding in protic, aprotic, and protein environments. *J. Am. Chem. Soc.* **144**, 7562–7567 (2022).
50. J. Dragelj, M. A. Mroginski, E. W. Knapp, Beating heart of cytochrome *c* oxidase: The shared proton of heme a_3 propionates. *J. Phys. Chem. B* **125**, 9668–9677 (2021).
51. L. Yang *et al.*, Water exit pathways and proton pumping mechanism in B-type cytochrome *c* oxidase from molecular dynamics simulations. *Biochim. Biophys. Acta* **1857**, 1594–1606 (2016).
52. X. Cai *et al.*, Identifying the proton loading site cluster in the ba_3 cytochrome *c* oxidase that loads and traps protons. *Biochim. Biophys. Acta Bioenerg.* **1861**, 148239 (2020).
53. X. Cai *et al.*, Network analysis of a proposed exit pathway for protons to the P-side of cytochrome *c* oxidase. *Biochim. Biophys. Acta Bioenerg.* **1859**, 997–1005 (2018).
54. A. L. Woelke *et al.*, Exploring the possible role of Glu286 in CcO by electrostatic energy computations combined with molecular dynamics. *J. Phys. Chem. B* **117**, 12432–12441 (2013).
55. B. M. Samudio, V. Couch, A. A. Stuchebrukhov, Monte Carlo simulations of Glu-242 in cytochrome *c* oxidase. *J. Phys. Chem. B* **120**, 2095–2105 (2016).
56. W. C. Kao *et al.*, Structural basis for safe and efficient energy conversion in a respiratory supercomplex. *Nat. Commun.* **13**, 545 (2022).
57. M. Svensson-Ek *et al.*, The X-ray crystal structures of wild-type and EQ(I-286) mutant cytochrome *c* oxidases from *Rhodobacter sphaeroides*. *J. Mol. Biol.* **321**, 329–339 (2002).
58. A. S. Pawate *et al.*, A mutation in subunit I of cytochrome oxidase from *Rhodobacter sphaeroides* results in an increase in steady-state activity but completely eliminates proton pumping. *Biochemistry* **41**, 13417–13423 (2002).
59. V. R. I. Kaila, M. I. Verkhovsky, G. Hummer, M. Wikström, Mechanism and energetics by which glutamic acid 242 prevents leaks in cytochrome *c* oxidase. *Biochim. Biophys. Acta* **1787**, 1205–1214 (2009).
60. F. Baserga *et al.*, Quantification of local electric field changes at the active site of cytochrome *c* oxidase by fourier transform infrared spectroelectrochemical titrations. *Front Chem.* **9**, 669452 (2021).
61. R. M. Nyquist, D. Heitbrink, C. Bolwien, R. B. Gennis, J. Heberle, Direct observation of protonation reactions during the catalytic cycle of cytochrome *c* oxidase. *Proc. Natl. Acad. Sci. U.S.A.* **100**, 8715–8720 (2003).
62. D. Okuno, T. Iwase, K. Shinzawa-Itoh, S. Yoshikawa, T. Kitagawa, FTIR detection of protonation/deprotonation of key carboxyl side chains caused by redox change of the $Cu_{(A)}$-heme *a* moiety and ligand dissociation from the heme a_3-$Cu_{(B)}$ center of bovine heart cytochrome *c* oxidase. *J. Am. Chem. Soc.* **125**, 7209–7218 (2003).
63. M. Iwaki, P. R. Rich, An IR study of protonation changes associated with heme-heme electron transfer in bovine cytochrome *c* oxidase. *J. Am. Chem. Soc.* **129**, 2923–2929 (2007).
64. V. Sharma, K. D. Karlin, M. Wikström, Computational study of the activated O_H state in the catalytic mechanism of cytochrome *c* oxidase. *Proc. Natl. Acad. Sci. U.S.A.* **110**, 16844–16849 (2013).
65. L. Noodleman *et al.*, Coupled transport of electrons and protons in a bacterial cytochrome *c* oxidase-DFT calculated properties compared to structures and spectroscopies. *Phys. Chem. Chem. Phys.* **22**, 26652–26668 (2020).
66. V. R. I. Kaila, M. P. Johansson, D. Sundholm, L. Laakkonen, M. Wiström, The chemistry of the CuB site in cytochrome *c* oxidase and the importance of its unique His-Tyr bond. *Biochim. Biophys. Acta* **1787**, 221–233 (2009).
67. M. R. A. Blomberg, Mechanism of oxygen reduction in cytochrome *c* oxidase and the role of the active site tyrosine. *Biochemistry* **55**, 489–500 (2016).
68. S. Buschmann *et al.*, The structure of cbb_3 cytochrome oxidase provides insights into proton pumping. *Science* **329**, 327–330 (2010).
69. V. Rauhamäki, D. A. Bloch, M. Wikström, Mechanistic stoichiometry of proton translocation by cytochrome cbb_3. *Proc. Natl. Acad. Sci. U.S.A.* **109**, 7286–7291 (2012).
70. V. Sharma, M. Wikström, V. R. I. Kaila, Dynamic water networks in cytochrome cbb_3 oxidase. *Biochim. Biophys. Acta* **1817**, 726–734 (2012).
71. C. A. Carvalheda, A. V. Pisliakov, Insights into proton translocation in cbb_3 oxidase from MD simulations. *Biochim. Biophys. Acta Bioenerg.* **1858**, 396–406 (2017).
72. H. J. Lee, R. B. Gennis, P. Ädelroth, Entrance of the proton pathway in cbb_3-type heme-copper oxidases. *Proc. Natl. Acad. Sci. U.S.A.* **108**, 17661–17666 (2011).

73. P. Saura, D. M. Frey, A. P. Gamiz-Hernandez, V. R. I. Kaila, Electric field modulated redox-driven protonation and hydration energetics in energy converting enzymes. *Chem. Commun. (Camb.)* **55**, 6078–6081 (2019).
74. V. R. I. Kaila, Long-range proton-coupled electron transfer in biological energy conversion: Towards mechanistic understanding of respiratory complex I. *J. R. Soc. Interface* **15**, 20170916 (2018).
75. F. Allgöwer, A. P. Gamiz-Hernandez, A. W. Rutherford, V. R. I. Kaila, Molecular principles of redox-coupled protonation dynamics in photosystem II. *J. Am. Chem. Soc.* **144**, 7171–7180 (2022).
76. N. G. Léonard, R. Dhaoui, T. Chantarojsiri, J. Y. Yang, Electric fields in catalysis: From enzymes to molecular catalysts. *ACS Catal.* **11**, 10923–10932 (2021).
77. A. D. Becke, Density-functional thermochemistry. III. The role of exact exchange. *J. Chem. Phys.* **98**, 5648–5652 (1993).
78. C. Lee, W. Yang, R. G. Parr, Development of the Colle-Salvetti correlation-energy formula into a functional of the electron density. *Phys. Rev. B Condens. Matter* **37**, 785–789 (1988).
79. R. B. Best *et al.*, Optimization of the additive CHARMM all-atom protein force field targeting improved sampling of the backbone φ, ψ and side-chain χ(1) and χ(2) dihedral angles. *J. Chem. Theory Comput.* **8**, 3257–3273 (2012).
80. M. P. Johansson, V. R. I. Kaila, L. Laakkonen, Charge parameterization of the metal centers in cytochrome *c* oxidase. *J. Comput. Chem.* **29**, 753–767 (2008).
81. S. G. Balasubramani *et al.*, TURBOMOLE: Modular program suite for ab initio quantum-chemical and condensed-matter simulations. *J. Chem. Phys.* **152**, 184107 (2020).
82. B. R. Brooks *et al.*, CHARMM: The biomolecular simulation program. *J. Comput. Chem.* **30**, 1545–1614 (2009).
83. S. Riahi, C. N. Rowley, The CHARMM-TURBOMOLE interface for efficient and accurate QM/MM molecular dynamics, free energies, and excited state properties. *J. Comput. Chem.* **35**, 2076–2086 (2014).
84. J. C. Phillips *et al.*, Scalable molecular dynamics on CPU and GPU architectures with NAMD. *J. Chem. Phys.* **153**, 044130 (2020).